

3D-PRINTED CONDENSERS WITH GRADIENT WICK STRUCTURES TO ENHANCE FILMWISE CONDENSATION

Mohammad Reza Shaeri¹, Sajjad Bigham², Vivek Mano Mohan², Maksym Demydovych¹

¹ Advanced Cooling Technologies, Inc., Lancaster, PA 17601

² Department of Mechanical and Aerospace Engineering, North Carolina State University, Raleigh, NC
27695

ABSTRACT

Enhancing filmwise condensation (FWC) of low-surface-tension fluids remains a challenge due to their extreme wetting properties. This study introduces an innovative 3D-printed metallic liquid-cooled condenser designed to improve FWC of low-surface-tension fluids. The condenser utilizes water to condense refrigerant R134a vapor, with the condenser featuring distinct sections for water and refrigerant, separated by a thin wall. The water side incorporates cylindrical pin fins, while the refrigerant side features capillary channels (wicks) with a two-dimensional gradient pore size distribution (2D-GPSD). This specialized wick design improves capillary-driven condensation by partially decoupling capillary pressure, permeability, and effective thermal conductivity of the wick-condensate. For comparison, a baseline condenser with identical geometry, water-side design, and porosity but with a uniform pore size wick was also 3D-printed, both constructed from stainless steel. Experiments were conducted under varying inlet water temperatures and refrigerant flow rates. The results demonstrated an improvement in FWC using the condenser with 2D-GPSD wicks, leading to an increase in condensation heat flux ranging from 26.7% to 54.5% under the inlet water temperatures tested in the present experiments.

Keywords: Filmwise condensation; Low-surface-tension fluids; Gradient wick structures; Additive manufacturing.

1. INTRODUCTION

The rapid and continuous miniaturization of electronic devices has generated an urgent demand for highly efficient and reliable thermal management technologies to maintain operating system and local temperatures within design limits [1–3]. Particularly, for high-heat-flux applications such as power electronic devices, which can experience heat flux above 1

kW/cm² [4,5], the focus has shifted to two-phase thermal management systems. Two-phase cooling, such as flow boiling, utilizes the latent heat of phase change, enabling a significantly higher heat transfer coefficient and a more uniform wall temperature distribution compared to single-phase cooling [6,7]. Flow boiling systems generally use boiling to absorb heat from the device and condensation to release heat from the working fluid and return it to a pre-boiling state [8]. As a result, the overall efficiency of two-phase cooling largely depends on improving both the boiling/evaporation and condensation processes. Additionally, improvements in boiling/evaporation and condensation result in the development of more compact evaporators and condensers, respectively, which are crucial for minimizing the Size, Weight, and Power (SWaP) of thermal management systems. However, compared to condensation, most research in this field has focused on boiling and evaporation, as a thorough understanding of heat transfer mechanisms in these processes is crucial for designing cooling systems that fit the specific dimensions of the devices being cooled [9]. For this reason, commercial condensers are often too large and inefficient [10]. As a result, effective techniques to enhance condensation heat transfer are highly needed to minimize the SWaP of thermal management systems [11].

Condensation can take place in two different modes: either as a continuous liquid film, known as filmwise condensation (FWC), or through the formation of droplets, referred to as dropwise condensation (DWC) [12]. DWC has already been identified as the preferred mode of condensation, offering heat transfer coefficients an order of magnitude higher than those in FWC [13]. However, FWC is the dominant mode of condensation in industrial-scale systems due to the high surface energy of commonly used metals [14]. Smooth hydrophobic surfaces, micro and nanostructured superhydrophobic surfaces, biphilic surfaces with patterned wettability, and lubricant-

infused surfaces have been used to promote DWC [15]. However, scaling durable surfaces that promote DWC to sustain condensation in practical applications remains a challenge [16,17]. Additionally, an extra challenge arises when the working fluid has low surface tension as common hydrophobic coated surfaces are ineffective at repelling these fluids, resulting in the wetting of these surfaces [17–19]. Low-surface-tension fluids like refrigerants are widely used in various industrial applications, such as chemical plants, natural gas production, food industry, and building energy technology [20]. As a result, developing effective techniques to enhance the FWC of low-surface-tension fluids is urgently required to minimize the SWaP of thermal management systems used in various industrial applications.

Enhanced condensation of low-surface-tension fluids is typically achieved through alternative techniques, such as using extended surfaces with fin designs or microchannels, which help reduce the thickness of the condensate film on the surfaces of the structures [19]. Wick structures also have been recognized as effective techniques for enhancing FWC [21]. Wicks enhance FWC by (i) providing larger condensation areas than a plain surface, and (ii) reducing the thermal resistance of the condensate-wick compared to that of a liquid film on a plain surface. We have recently developed a copper 3D-printed wicked condenser and demonstrated a significant enhancement in the stationary FWC of HFE-7100, a low-surface-tension fluid, compared to a bare copper surface [22].

In the present study, we are extending the use of wick structures to enhance FWC in the flow condensation of low-surface-tension fluids. However, fabricating the proposed wicks using traditional manufacturing techniques presents significant challenges. Additive manufacturing, also known as 3D printing, overcomes the fabrication challenges of traditional manufacturing techniques in terms of design complexity and internal structure, capabilities that traditional manufacturing processes cannot easily match [23–25]. This paper introduces a 3D-printed liquid-cooled condenser made of stainless steel, designed to enhance FWC of low-surface-tension fluids. Water is used as the coolant to condense the vapor of refrigerant R134a. The innovative aspect of the condenser lies in its refrigerant side, which features wick structures with gradient pore size distributions in two dimensions. As the baseline for comparison, the performance of the condenser is compared to an identical condenser with a uniform pore size distribution, while maintaining the same porosity in both condensers.

2. EXPERIMENT

2.1 3D Printing of Condensers

The condenser fabricated in this study comprises two main sections: the condenser and the coolant section, referred to as the refrigerant side and the water side, respectively, throughout this report. These two sections are positioned opposite each other and are separated by a 1.6 mm thick wall. The refrigerant vapor enters the condenser, where it undergoes phase change due to the cooling provided by the circulating water on the coolant side. Figure 1 illustrates the 3D-printed condenser before the inlet and

outlet manifolds are welded. The condenser's trapezoidal footprint was selected to enhance its compactness, which remains the focus of our ongoing research. However, alternative geometries, such as a rectangular footprint, can also be employed. The design includes separate inlet and outlet manifolds for both the refrigerant and coolant sides, each with a diameter of 6.35 mm. The separate inlet and outlet manifolds facilitate the study of cocurrent and counter-current flow, corresponding to parallel and opposite flow directions of the working fluids, respectively. In this study, the condenser operates under a cocurrent flow arrangement, as our initial tests indicated better performance with this configuration.

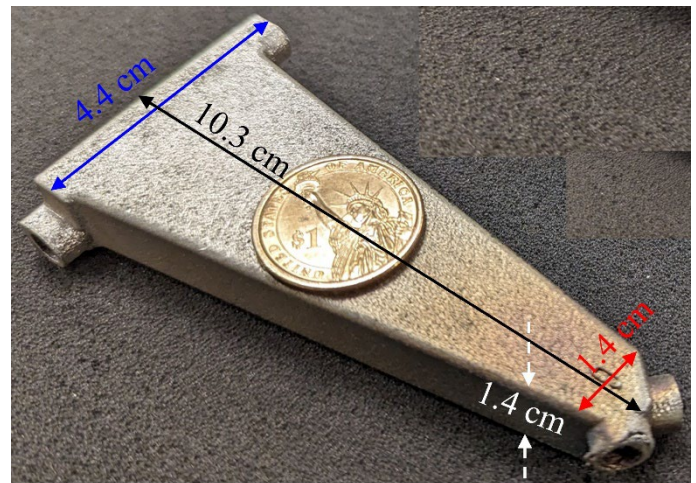


Figure 1: 3D-printed condenser, made of stainless steel.

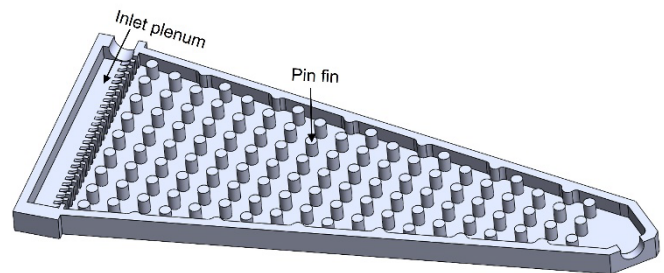


Figure 2: CAD model of the coolant side (i.e., water side).

Figure 2 shows the CAD model of the coolant side (i.e., the water side), which features cylindrical pin fins with a diameter of 1.5 mm, a height of 4.76 mm, and a center-to-center spacing of 3.5 mm.

On the refrigerant side, there are two alternating converging capillary structures (wicks) and an outlet wick. Each wick is surrounded by two empty spaces. The outlet wick connects all individual wicks to (i) maintain continuity in capillary pressure and the liquid meniscus at the condenser outlet, and (ii) prevent the bypass of refrigerant vapor. The innovation of the proposed condenser lies in its refrigerant-side design, which incorporates gradient lattice wick structures with decreasing pore sizes from the condenser inlet to the outlet, as well as from the wick center

to its edges. This capillary structure is termed a two-dimensional gradient pore size distribution (2D-GPSD) wick. The wick structure has a height of 4.76 mm and a wall thickness of 300 μm . The schematic representation of the 2D-GPSD wick development is shown in Figure 3, where each color indicates a distinct zone with a unique pore size. The pore sizes decrease from zone 1 (blue), which has the largest pores, to zone 7 (brown), which has the smallest. In the condenser examined in this study, the pore sizes range from 900 μm in zone 1 to 300 μm in zone 7, decreasing in increments of 100 μm .

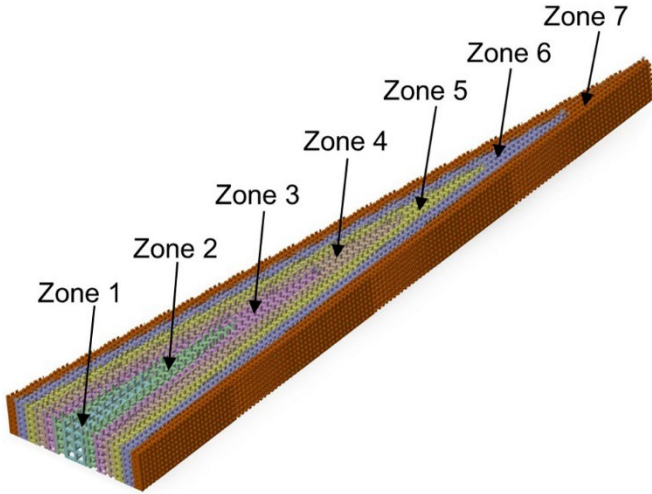


Figure 3: Concept to illustrate the two-dimensional gradient pore size distribution (2D-GPSD) on the refrigerant side.

The proposed condenser with 2D-GPSD wicks advances capillary-driven condensation beyond the current state-of-the-art by enhancing capillary pressure (P_{cap}), wick permeability (μ), and the effective thermal conductivity of the wick-condensate (k_{eff}), while also delaying flooding. The performance of capillary-driven condensation improves with higher P_{cap} , μ , and k_{eff} . However, in a homogeneous wick with a fixed pore size, P_{cap} and k_{eff} are inversely related to μ , as such while smaller pore sizes increase P_{cap} and k_{eff} , they reduce μ . A lower μ leads to a higher viscous pressure drop within the wick (ΔP_{wick}) and an increased likelihood of flooding, which negatively impacts condensation heat transfer. Flooding occurs when ΔP_{wick} exceeds P_{cap} . To address the trade-offs among P_{cap} , k_{eff} , and μ , wicks with gradient pore size distributions have been shown to partially decouple these competing factors, thereby improving the overall performance of capillary-driven condensation [26].

Furthermore, the topology of the proposed condenser and its capillary channels contributes to reducing ΔP_{wick} , thereby aiding to prevent flooding. At a given cross-section within the capillary channel, the corresponding ΔP_{wick} for the lateral transport of liquid into each empty space is expressed as follows [27]:

$$\Delta P_{\text{wick}} = (\mu L \dot{m}) / (\rho k A) \quad (1)$$

where L represents the length for lateral liquid transport through the wick, and \dot{m} corresponds to the liquid mass flow rate. Since each capillary channel is surrounded by two empty spaces, the liquid is drawn laterally from both sides of the wick into these empty spaces, effectively splitting both L and \dot{m} approximately in half.

The refrigerant vapor and cold water enter their respective main inlet manifolds and subsequently flow through the refrigerant and water layers. At the inlet of the condenser, cold water enters the water side, providing cooling for the condensation of refrigerant vapor on the refrigerant side, and exits the water side at a higher temperature. On the refrigerant side, refrigerant vapor enters capillary channels with relatively large pores. Within each channel, condensation occurs inside the wicks, and the liquid is laterally transported to two adjacent empty spaces due to P_{cap} . That part of vapor flowing inside the empty spaces is also condensed on the vertical walls of the capillary channels and the horizontal plain surface. As the distance from the inlet increases, the amount of condensate gradually rises, eventually leading to a state where near the outlet is predominantly filled with liquid. The accumulated liquid is then drawn through the outlet wick and is pumped outside the condenser.

The performance of the condenser featuring 2D-GPSD wicks was compared with a baseline condenser that has identical dimensions and water-side configuration, as well as the same refrigerant-side porosity, but with a uniform pore size. Throughout the remainder of this paper, this baseline condenser is referred to as the UPSD condenser, which denotes a Uniform Pore Size Distribution. The porosity of the condenser with 2D-GPSD on the refrigerant side was calculated from its CAD model and found to be approximately 73.8%. At this porosity, the equivalent pore size for the UPSD condenser is 570 μm . An X-ray image of each condenser is illustrated in Figure 4, showing the 2D-GPSD and UPSD wicks on the refrigerant sides, as well as the pin fins on the water sides of each condenser. Figure 5 illustrates the interior of the refrigerant sides of two condensers and their water sides after the top surfaces of both condensers were removed using wire EDM (Electrical Discharge Machining) cut.

The condensers were manufactured through one single 3D printing process using a GE Concept Laser 3D printer with 17-4PH stainless steel. An in-house methanol bath was developed, and the condensers were continuously flushed with methanol to remove any excess powder remaining inside both the refrigerant and water sides. The powder removal process was repeated multiple times, with each cycle lasting an adequate amount of time. Once the powder removal was complete, the main inlet and outlet manifolds for the water and refrigerant sides were welded to the respective inlet and outlet tubes.

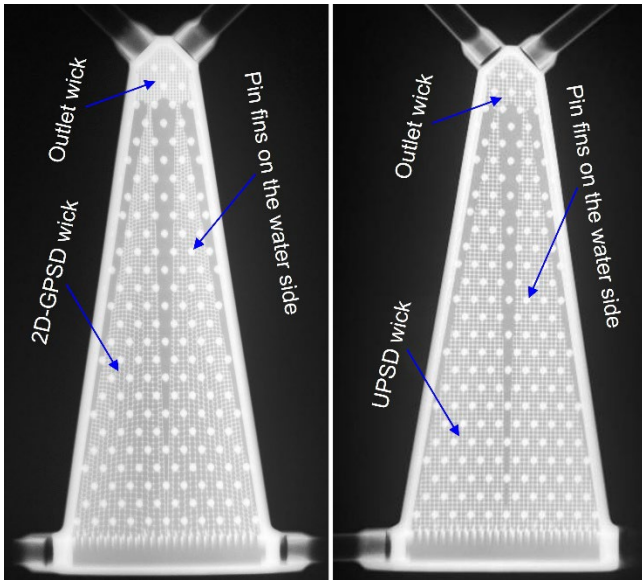


Figure 4: X-ray images of the condensers. (left) 2D-GPSD wicks, (right) UPSD wicks.

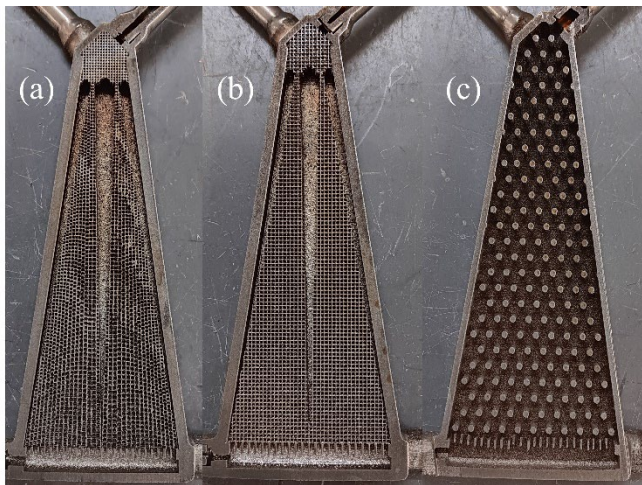


Figure 5: The interior section of (a) the refrigerant side with 2D-GPSD wicks, (b) the refrigerant side with UPSD wicks, and (c) the water side.

2.2 Experiment

A refrigeration condensation loop integrated with a water-cooled loop was fabricated to perform flow condensation tests. Figure 6 shows a simplified schematic of the experimental setup, where all components were interconnected using stainless steel tubing. The refrigerant loop includes multiple heat exchangers positioned upstream and downstream of the condenser, as well as T-type thermocouples, flowmeters, pressure transducers, control valves, and a positive displacement pump. The refrigerant flow rate to the condenser was regulated via a control valve and bypass installed after the pump, with measurements taken by a flowmeter located upstream of the condenser inlet. A heater was incorporated into the upstream of the condenser inlet

to achieve the specified thermodynamic conditions, such as ensuring the refrigerant enters the condenser in a superheated state. Pressure at the refrigerant inlet was measured using an absolute pressure transducer, while a differential pressure transducer (DPT) recorded the pressure drop across the refrigerant side. Sight glasses were installed at both the inlet and outlet of the refrigerant side to visualize the flow. The water-cooled loop was equipped with T-type thermocouples at both the inlet and outlet of the condenser's water side, a DPT to measure the pressure drop across the water side, a flowmeter, a control valve to adjust the water flow rate, and a chiller that circulated the water and maintained the inlet water temperature.

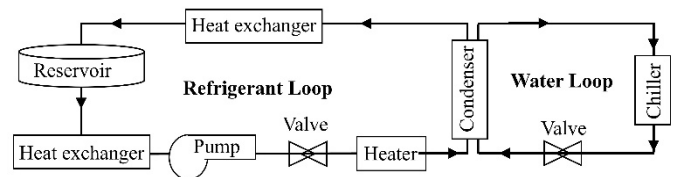


Figure 6: Schematic of the flow condensation loop.

The hermeticity of the individual refrigerant and water sides of the condenser was checked by a helium mass spectrometer with a measured leak rate less than 9×10^{-10} Std. cc/s [28,29]. Following this, the condenser was inserted into the loop. Before starting the experiments, the entire loop was checked for leaks prior to charging it with R134a. Once the liquid was circulated through the loop, the pump speed and control valve were adjusted to achieve the desired refrigerant flow rate to the condenser. The chiller temperature on the refrigerant side was maintained at 20°C throughout the experiments. By regulating the chiller temperature on the water side, the inlet water temperature to the condenser was controlled. To reduce heat exchange with the surrounding environment, the entire condenser was insulated. The outlet of the refrigerant side may still contain two-phase flow; therefore, several heat exchangers, particularly before the pump, were incorporated to ensure the inlet fluid to the pump remains subcooled, thereby preventing cavitation. The voltage of the variable transformer powering the heater was adjusted to ensure that the refrigerant entering the condenser was superheated, preventing any liquid refrigerant from entering the condenser. The degree of superheat was determined by measuring the inlet temperature and pressure of the refrigerant and subtracting the corresponding saturation temperature at the inlet pressure from the measured inlet temperature. In this study, all experiments were conducted with an inlet superheat of less than 2.3 °C. The tests were performed at three different inlet water temperatures: 5 °C, 10 °C, and 15 °C, with a fixed water flow rate of 0.58 LPM (liter per minute) and three different refrigerant mass flow rates of 0.5 g/s, 1 g/s, and 1.6 g/s. LabVIEW was used to integrate hardware components and collect data from the thermocouples, pressure transducers, and flowmeters in both the flow condensation loop and water loop once the system reached steady-state conditions. Steady-state conditions were determined when the temperature

variations, as measured by the T-type thermocouples, remained below 0.5 °C during 10 minutes of system operation.

2.3 Data Reduction

Since the focus of this study is not on the water side, the hydrothermal performance of the water side is not investigated here and will be the subject of our future research. The results in this study are presented in terms of the condensation heat flux (q''), the exit vapor quality of the refrigerant (x_e), and the pressure drop across the refrigerant side (ΔP_R).

The cooling power provided from the water flow to the condenser (\dot{Q}) is calculated as follows:

$$\dot{Q} = \dot{m}_w(h_{o,w} - h_{i,w}) \quad (2)$$

where \dot{m}_w , $h_{o,w}$, and $h_{i,w}$ stand for the mass flow rate of water, outlet specific enthalpy of water, and inlet specific enthalpy of water, respectively. The q'' is calculated as the ratio of the \dot{Q} and the projected area of the refrigerant side, as follows:

$$q'' = \dot{Q}/A_R \quad (3)$$

where A_R denotes the projected area of the refrigerant layer. The projected area was determined using the CAD model of the condenser. The x_e is calculated as follows:

$$x_e = 1 - \frac{\dot{m}_c}{\dot{m}_R} \quad (4)$$

where \dot{m}_R is the mass flow rate of refrigerant, and \dot{m}_c represents the condensate mass flow rate, which is calculated as follows:

$$\dot{m}_c = \frac{\dot{Q} - \dot{m}_R c_{p,R} \Delta T_{sup,i}}{h_{fg}} \quad (5)$$

where \dot{m}_R and $c_{p,R}$ are the refrigerant mass flow rate and specific heat, respectively. Also, $\Delta T_{sup,i}$ and h_{fg} represents the inlet superheat temperature and the latent heat of vaporization, respectively. The pressure drop across the refrigerant side, ΔP_R , was directly measured using a DPT placed between the main inlet and outlet of the refrigerant side.

3 RESULTS AND DISCUSSION

The condensation tests were conducted with the condensers operating in a horizontal orientation. In this section, q'' , x_e , and ΔP_R for both condensers at various \dot{m}_R and inlet water temperature ($T_{in,w}$) are illustrated and discussed. In each graph, (U) and (G) in the figure legend represent the condenser with UPSD and the condenser with 2D-GPSD, respectively.

Figure 7 compares q'' between two condensers. For a given inlet water temperature and condenser, increasing the refrigerant flow rate leads to a higher q'' , due to enhanced convective heat

transfer on the refrigerant side. For a given condenser and refrigerant flow rate, q'' increases as the water inlet temperature decreases. This is due to a rise in the subcooled temperature resulting from a lower water inlet temperature. As a notable achievement, the condenser with 2D-GPSD provides a significantly higher q'' compared to the condenser with UPSD. Under the inlet water temperatures tested in the present experiments, the condenser with 2D-GPSD increased q'' by 26.7% to 35.4% at the lowest refrigerant flow rate, 31.8% to 40.2% at the middle refrigerant flow rate, and 40% to 54.5% at the highest refrigerant flow rate.

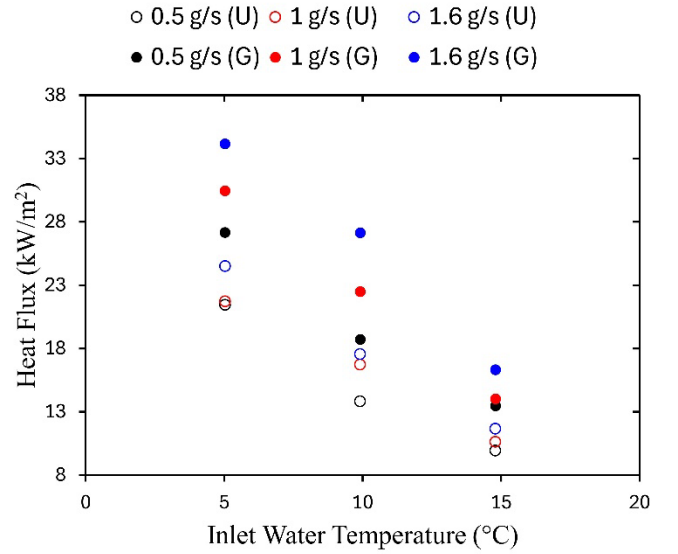


Figure 7: Condensation heat flux at different refrigerant mass flow rates and inlet water temperatures.

Figure 8 compares x_e for both condensers. For a given condenser and refrigerant mass flow rate, x_e decreases with a lower inlet water temperature, as the reduced temperature enhances condensation. A key observation from this figure is that (i) neither condenser achieved full condensation under any operating condition, and (ii) for a given condenser and inlet water temperature, increasing the refrigerant flow rate leads to a higher x_e (i.e., reduced condensation). This indicates the existence of a threshold refrigerant flow rate required for full condensation, dependent on condenser design and operating conditions such as refrigerant flow rate and inlet water temperature. Understanding this threshold is crucial to avoiding oversized condensers, which would otherwise increase SWaP. Ongoing research within our team focuses on optimizing condenser design to achieve full condensation across a wider range of flow rates. Overall, as expected due to the enhanced FWC provided by the condenser with 2D-GPSD, this condenser achieved higher condensation compared to the condenser with UPSD at a given refrigerant flow rate and inlet water temperature. Under the inlet water temperatures tested in the present experiments, the condenser with 2D-GPSD reduced x_e by 11.7% to 30.6% at the lowest refrigerant flow rate, 5% to

14.5% at the middle refrigerant flow rate, and 4% to 9.4% at the highest refrigerant flow rate.

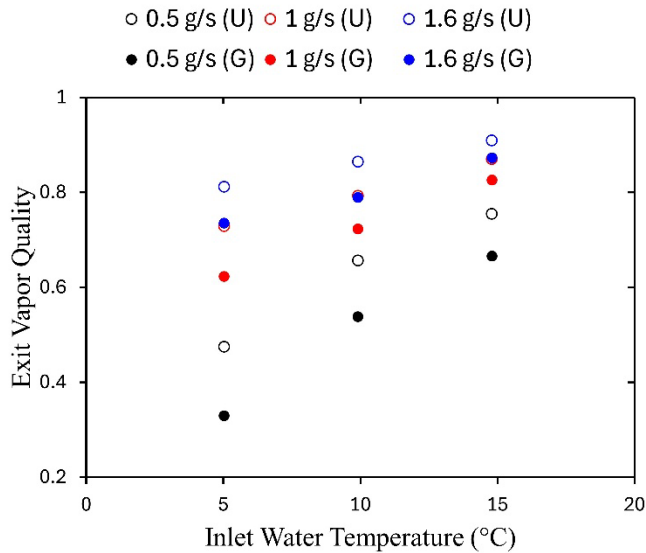


Figure 8: Exit vapor quality at different refrigerant mass flow rates and inlet water temperatures.

Figure 9 illustrates ΔP_R for both condensers at different refrigerant flow rates and inlet water temperatures. ΔP_R for the condenser with UPSD could not be measured accurately because they were too small for the current DPT used in the experiments. In future tests, a DPT with a lower range will be used to accurately measure the low-range pressure drops. As a result, this study discusses only ΔP_R associated with the condenser with 2D-GPSD wick. At a given flow rate and inlet water temperature, the condenser with 2D-GPSD wicks experienced a higher ΔP_R compared to the condenser with UPSD wicks. This is most likely due to the smaller pore sizes in the 2D-GPSD structure, leading to reduced permeability and, consequently, a larger ΔP_R . Additionally, at a given inlet water temperature, increasing the flow rate leads to a higher ΔP_R due to higher vapor velocity. At a fixed refrigerant flow rate, the ΔP_R decreases with a lower water inlet temperature. This is because a lower inlet temperature leads to reduced x_e (i.e., more condensate), which subsequently lowers the ΔP_R .

In summary, the 3D-printed wicked condenser with gradient pore size distributions demonstrated a strong concept and can serve as a promising technique for enhancing FWC of low-surface-tension fluids in industrial applications. Further research is needed to improve the performance of the proposed condenser, as outlined in the “Future Work” section.

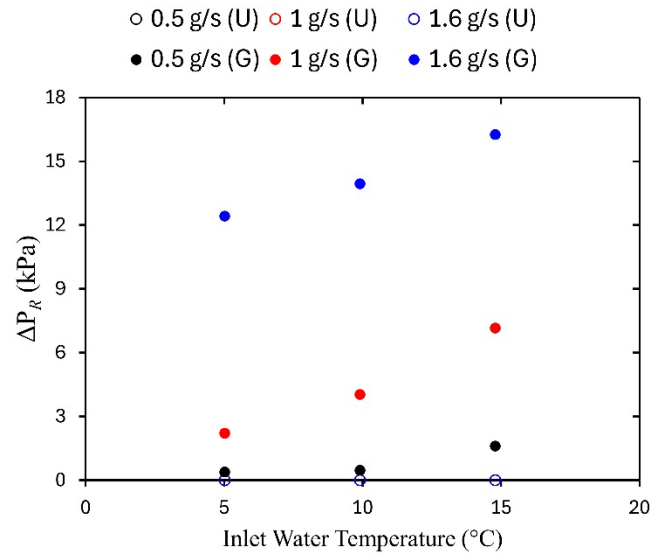


Figure 9: Pressure drops across the refrigerant side of the condensers at different refrigerant mass flow rates and inlet water temperatures.

4 CONCLUSION

This study introduced a 3D-printed liquid-cooled condenser made of stainless steel to enhance FWC of low-surface-tension fluids. Water was utilized as the coolant for condensing the refrigerant vapor of R134a. The innovative aspect of the condenser is its refrigerant side, which incorporates wick structures with 2D-GPSD. Experimental results showed that compared to the baseline condenser featuring uniform wick structures, the condenser with 2D-GPSD significantly enhanced the condensation heat flux.

5 FUTURE WORK

The present study is still in the preliminary phase of research. Future work focusing on optimizing the pore size distributions on the refrigerant side and enhancing heat transfer characteristics on the water side is anticipated to further improve the hydrothermal performance of the proposed condenser, making it a promising solution for reducing the SWaP of future thermal management systems. Additionally, for the fabrication of scaled-up designs, challenges such as the development of efficient manifold designs to prevent flow maldistribution should be addressed through comprehensive computational and experimental studies.

ACKNOWLEDGEMENTS

This material is based upon work supported by the Office of Naval Research under Contract No. N68335-23-C-0464. The support of Dr. Mark Spector from the Office of Naval Research is gratefully acknowledged.

REFERENCES

- [1] Camarasa, J., Vilarrubí, M., Ibáñez, M., Rosell, P., Beberide, D., and Barrau, J., “Experimental Study of

- Flow Boiling Cooling in a Novel Variable Density Pin-Fin Device,” *Applied Thermal Engineering*, Vol. 269, 2025, p. 126023. <https://doi.org/10.1016/j.applthermaleng.2025.126023>
- [2] Shaeri, M. R., and Demydovych, M., “Thermal Management of Multiple High-Heat-Flux Heat Sources Using Additively Manufactured Two-Phase Cold Plate,” presented at the 2024 23rd IEEE Intersociety Conference on Thermal and Thermomechanical Phenomena in Electronic Systems (ITherm), Aurora, CO, USA, 2024. <https://doi.org/10.1109/ITherm55375.2024.10709620>
- [3] Parizad Benam, B., Sadaghiani, A. K., Yağcı, V., Parlak, M., Sefiane, K., and Koşar, A., “Review on High Heat Flux Flow Boiling of Refrigerants and Water for Electronics Cooling,” *International Journal of Heat and Mass Transfer*, Vol. 180, 2021, p. 121787. <https://doi.org/10.1016/j.ijheatmasstransfer.2021.121787>
- [4] Yang, S., Li, J., Cao, B., Wu, Z., and Sheng, K., “Investigation of Z-Type Manifold Microchannel Cooling for Ultra-High Heat Flux Dissipation in Power Electronic Devices,” *International Journal of Heat and Mass Transfer*, Vol. 218, 2024, p. 124792. <https://doi.org/10.1016/j.ijheatmasstransfer.2023.124792>
- [5] Abo-Zahhad, E. M., Amine Hachicha, A., Said, Z., Ghenai, C., and Ookawara, S., “Thermal Management System for High, Dense, and Compact Power Electronics,” *Energy Conversion and Management*, Vol. 268, 2022, p. 115975. <https://doi.org/10.1016/j.enconman.2022.115975>
- [6] Cao, B., Li, J., Wu, Z., and Sheng, K., “Flow Boiling in Novel Radial Microchannels for Cooling of Electronic Devices and Modules of Annular Temperature Distribution,” *International Journal of Heat and Mass Transfer*, Vol. 239, 2025, p. 126555. <https://doi.org/10.1016/j.ijheatmasstransfer.2024.126555>
- [7] Shaeri, M. R., Chen, C.-H., Bonner, R. W., and Demydovych, M., “Demonstration of CTE-Matched Two-Phase Minichannel Heat Sink,” Orlando, FL, USA, 2023. <https://doi.org/10.1109/ITherm55368.2023.10177605>
- [8] O’Neill, L. E., Mudawar, I., Hasan, M. M., Nahra, H. K., Balasubramaniam, R., and Mackey, J. R., “Flow Condensation Pressure Oscillations at Different Orientations,” *International Journal of Heat and Mass Transfer*, Vol. 127, 2018, pp. 784–809. <https://doi.org/10.1016/j.ijheatmasstransfer.2018.07.072>
- [9] O’Neill, L. E., Balasubramaniam, R., Nahra, H. K., Hasan, M. M., and Mudawar, I., “Flow Condensation Heat Transfer in a Smooth Tube at Different Orientations: Experimental Results and Predictive Models,” *International Journal of Heat and Mass Transfer*, Vol. 140, 2019, pp. 533–563. <https://doi.org/10.1016/j.ijheatmasstransfer.2019.05.103>
- [10] Zhou, L., Garg, D., Qiu, Y., Kim, S.-M., Mudawar, I., and Kharangate, C. R., “Machine Learning Algorithms to Predict Flow Condensation Heat Transfer Coefficient in Mini/Micro-Channel Utilizing Universal Data,” *International Journal of Heat and Mass Transfer*, Vol. 162, 2020, p. 120351. <https://doi.org/10.1016/j.ijheatmasstransfer.2020.120351>
- [11] Derby, M. M., Chatterjee, A., Peles, Y., and Jensen, M. K., “Flow Condensation Heat Transfer Enhancement in a Mini-Channel with Hydrophobic and Hydrophilic Patterns,” *International Journal of Heat and Mass Transfer*, Vol. 68, 2014, pp. 151–160. <https://doi.org/10.1016/j.ijheatmasstransfer.2013.09.024>
- [12] El Fil, B., Kini, G., and Garimella, S., “A Review of Dropwise Condensation: Theory, Modeling, Experiments, and Applications,” *International Journal of Heat and Mass Transfer*, Vol. 160, 2020, p. 120172. <https://doi.org/10.1016/j.ijheatmasstransfer.2020.120172>
- [13] Thomas, T. M., Sinha Mahapatra, P., Ganguly, R., and Tiwari, M. K., “Preferred Mode of Atmospheric Water Vapor Condensation on Nanoengineered Surfaces: Dropwise or Filmwise?,” *Langmuir*, Vol. 39, No. 15, 2023, pp. 5396–5407. <https://doi.org/10.1021/acs.langmuir.3c00022>
- [14] Liu, Z., and Preston, D. J., “Enhanced Condensation for Improved Energy Efficiency,” *Joule*, Vol. 3, No. 5, 2019, pp. 1182–1184. <https://doi.org/10.1016/j.joule.2019.04.008>
- [15] Ahlers, M., Buck-Emden, A., and Bart, H.-J., “Is Dropwise Condensation Feasible? A Review on Surface Modifications for Continuous Dropwise Condensation and a Profitability Analysis,” *Journal of Advanced Research*, Vol. 16, 2019, pp. 1–13. <https://doi.org/10.1016/j.jare.2018.11.004>
- [16] Philander, E., Kawaguchi, T., and Saito, T., “Dropwise Condensation Performance of Sprayable Polymer/Copper Oxide Composite Coating,” *International Journal of Heat and Mass Transfer*, Vol. 234, 2024, p. 126101. <https://doi.org/10.1016/j.ijheatmasstransfer.2024.126101>
- [17] Ho, J. Y., Rabbi, K. F., Sett, S., Wong, T. N., and Miljkovic, N., “Dropwise Condensation of Low Surface Tension Fluids on Lubricant-Infused Surfaces: Droplet Size Distribution and Heat Transfer,” *International Journal of Heat and Mass Transfer*, Vol. 172, 2021, p. 121149. <https://doi.org/10.1016/j.ijheatmasstransfer.2021.121149>

- [18] Zhao, Y., “Dropwise Condensation of Water and Low Surface Tension Fluids on Structured Surfaces,” 2018. <https://doi.org/10.1016/j.icheatmasstransfer.2020.104490>
- [19] Aili, A., Ge, Q., and Zhang, T., “Condensation of Low-Surface-Tension Fluids on Microstructured Surfaces at Low Temperature,” presented at the ASME 2017 International Mechanical Engineering Congress and Exposition, Tampa, Florida, USA, 2017. <https://doi.org/10.1115/IMECE2017-71675>
- [20] Sett, S., Yan, X., Barac, G., Bolton, L. W., and Miljkovic, N., “Lubricant-Infused Surfaces for Low-Surface-Tension Fluids: Promise versus Reality,” *ACS Applied Materials & Interfaces*, Vol. 9, No. 41, 2017, pp. 36400–36408. <https://doi.org/10.1021/acsami.7b10756>
- [21] Preston, D. J., Wilke, K. L., Lu, Z., Cruz, S. S., Zhao, Y., Becerra, L. L., and Wang, E. N., “Gravitationally Driven Wicking for Enhanced Condensation Heat Transfer,” *Langmuir*, Vol. 34, No. 15, 2018, pp. 4658–4664. <https://doi.org/10.1021/acs.langmuir.7b04203>
- [22] Saple, J., Ahmadi, B., Shaeri, M. R., and Bigham, S., “Experimental Study of a 3D-Printed Wick Condenser for Enhanced Condensation Heat Transfer,” presented at the 2024 23rd IEEE Intersociety Conference on Thermal and Thermomechanical Phenomena in Electronic Systems (ITherm), Aurora, CO, USA, 2024. <https://doi.org/10.1109/ITherm55375.2024.10709465>
- [23] Shaeri, M. R., and Demydovych, M., “3D Printed Capillary-Driven Cold Plate for Hybrid Two-Phase Cooling System,” presented at the ASME 2024 Heat Transfer Summer Conference collocated with the ASME 2024 Fluids Engineering Division Summer Meeting and the ASME 2024 18th International Conference on Energy Sustainability, Anaheim, California, USA, 2024. <https://doi.org/10.1115/HT2024-121704>
- [24] Geng, Z., and Bidanda, B., “Geometric Precision Analysis for Additive Manufacturing Processes: A Comparative Study,” *Precision Engineering*, Vol. 69, 2021, pp. 68–76. <https://doi.org/10.1016/j.precisioneng.2020.12.022>
- [25] Shaeri, M. R., Demydovych, M., and Chen, C.-H., “Additively Manufactured Cold Plate Integrated With Evaporator Wicks and Phase Separators for Thermal Management of Multiple High-Heat-Flux Heat Sources,” presented at the ASME 2024 International Technical Conference and Exhibition on Packaging and Integration of Electronic and Photonic Microsystems, San Jose, California, USA, 2024. <https://doi.org/10.1115/IPACK2024-141775>
- [26] Durgam, G. V., “Capillary-Assisted Enhanced Condensation Heat Transfer for Low Surface Tension Liquids,” 2018.
- [27] Shaeri, M. R., Bonner, R. W., and Ellis, M. C., “Thin Hybrid Capillary Two-Phase Cooling System,” *International Communications in Heat and Mass Transfer*, Vol. 112, 2020, p. 104490.
- [28] Shaeri, M. R., Attinger, D., and Bonner, R. W., “Vapor Chambers with Hydrophobic and Biphilic Evaporators in Moderate to High Heat Flux Applications,” *Applied Thermal Engineering*, Vol. 130, 2018, pp. 83–92. <https://doi.org/10.1016/j.applthermaleng.2017.11.051>
- [29] Ju, Y. S., Kaviany, M., Nam, Y., Sharratt, S., Hwang, G. S., Catton, I., Fleming, E., and Dussinger, P., “Planar Vapor Chamber with Hybrid Evaporator Wicks for the Thermal Management of High-Heat-Flux and High-Power Optoelectronic Devices,” *International Journal of Heat and Mass Transfer*, Vol. 60, 2013, pp. 163–169. <https://doi.org/10.1016/j.ijheatmasstransfer.2012.12.058>